Single exposure lensless subpixel phase imaging

Péter Kocsis, Igor Shevkunov, Vladimir Katkovnik, and Karen Egiazarian

Faculty of Information Technology and Communication Sciences, Tampere University, P.O. Box 553, FI-33101 Tampere, Finland

ABSTRACT

Lensless phase-retrieval system with phase modulation of free propagation wavefront is proposed. Contrary to the traditional super-resolution phase-retrieval, the method in this paper requires a single observation only and uses advanced SR-SPAR iterative technique. Successful object imaging relies on modulation of the object wavefront with a random phase-mask, which generates enlarged intensity patterns, allowing us to extract more information than it is possible without such a mask. The achieved high-quality super-resolution phase-imaging is demonstrated by simulation-tests produced with the parameters corresponding to the physical prototype of the considered optical system.

Keywords: phase imaging, phase retrieval, sub-pixel resolution, sparse representation, lensless imaging, lensless system design, phase measurement, diffractive optical element

1. INTRODUCTION

The high resolution reconstruction of the complex wavefront is a significantly important part in microscopy because a large number of biological specimens like red blood cells, tissues, etc. are subjects of study.[1,2] These objects can not be analyzed by traditional microscopy without special preparation of specimen, because amplitude characteristics do not provide enough information on their properties and internal structure. This missing information can be obtained by reconstructing object's phase characteristics, although the problem of the phase recovery is that we can measure only the intensity of the light radiation. There are two main ways to extract phase information from the captured intensity either by using a holography,[3] or so-called phase retrieval techniques.[4–6] The former is invented by Gábor Dénes around 1948, it is well-known technique which allows phase reconstruction from holograms (interference patterns between object and reference beams); while the latter typically assumes free-space propagation between the object and the capturing device without reference beams, and uses iterative procedures to reconstruct the object from the captured diffraction patterns. These patterns are results of images overlapping of first-, zero-, and inverse diffraction orders. As a result of this overlapping, less information can be retrieved from a single pattern, but recording several different diffraction patterns can provide information sufficient for the phase reconstruction.[7] A necessary redundancy of multiple observations can be generated by moving[8] or rotating[9] optical elements (sensor or object), by modulating wavefronts by using multi-wavelength illumination[10,11] or by special programmable optical elements, for example, spatial light modulators (SLM).[12,13]

In contradistinction to these techniques, in this paper, a single-exposure phase-retrieval is demonstrated. By using a random modulation phase-mask located between object and sensor planes, we enlarge narrow diffraction patterns to spread across the sensor, gaining more information from the wavefront. However, the reconstruction from this enlarged pattern can cause corruption in phase, therefore an effective filtering is required. We apply the block-matching 3D[14] (BM3D) filter that already provided good results for several optical problems in previous researches.[15,16]

Traditionally for super-resolution imaging in multi-observation case, the recorded patterns can be combined to create an up-sampled pattern, which from super-resolved image of the object is retrievable.[17–20] Although in the single observation case only one captured pattern is assumed, we can use up-sampling techniques developed for image processing[21,22] to gain the required sub-pixel resolution. In this paper, we follow a different approach

Further author information: (Send correspondence to Péter Kocsis)
Péter Kocsis: E-mail: peter.kocsis@tuni.fi

based on modeling of optical image formation and registration. The corresponding Super Resolution Sparse Phase Amplitude Retrieval (SR-SPAR) algorithm[23,24] is modified and tuned for a single observation.

The contribution of this paper concerns the design of the optical system including wavefront modulation for a single observation setup with a single binary random phase mask, and also the optimization of the SR-SPAR algorithm used for object reconstruction from a registered diffraction pattern. The paper is focused on simulation of this super-resolution imaging system including proper selection of the object-mask and mask-sensor distances, as well as the phase-mask properties. It is shown, that the designed system can provide the quality of sub-pixel imaging up to the computational super-resolution factor of 6. Further advantage is that our method is lensless, which means that the system is compact and free from optical lens aberrations, furthermore, provides much larger field of view.[25–29]

2. METHOD DESCRIPTION

2.1 Observation formation

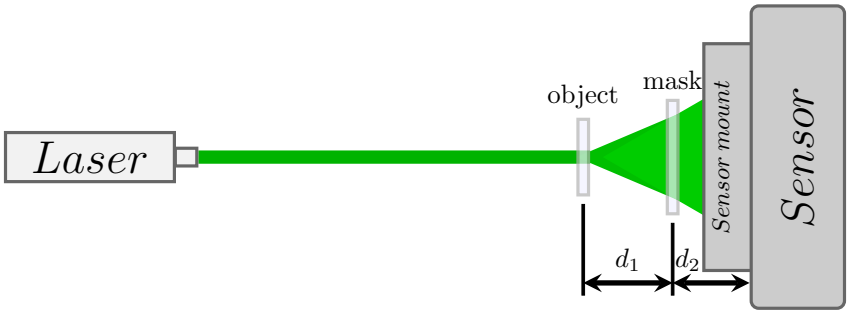

Figure 1. Lensless optical setup with phase-mask and laser illumination, the object-mask distance is d_1 and mask-sensor distance is d_2.

The proposed optical setup (Fig. 1) contains a laser source with a wavelength λ, test object, phase-mask, and mounted CMOS sensor. The captured intensity of the propagated wavefront can be written as

$$z = \left| P_{d_2} \left\{ M \circ P_{d_1} \left\{ u_o \right\} \right\} \right|^2, \tag{1}$$

where $u_o \in \mathbb{C}^{N\times N}$ is the $N\times N$ complex-valued object wavefront (wavefront just behind the object plane), which is propagated forward to the mask plane. The wavefront after the mask can be written as the entry-wise (Hadamard) product of the $M \in \mathbb{C}^{N\times N}$ phase mask and the propagated object wavefront with the mask-object distance d_1. This complex wavefront then propagated toward the sensor with the distance d_2, where it is captured as intensity measurement $z \in \mathbb{R}_+^{N\times N}$ of the size $N \times N$. $P_d : \mathbb{C}^{N\times N} \mapsto \mathbb{C}^{N\times N}$ stands for the free space forward propagation operator on the distance d.

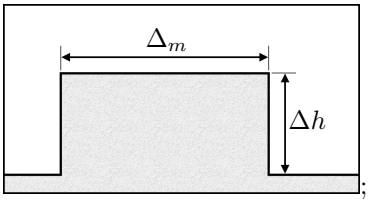

Figure 2. Cross-section of a pixel fragment of an ideal binary phase-mask, with pixel size of Δ_m and height of Δh

In Fig. 2, we show a cross-section fragment of the used binary phase-mask, illustrating the shape of the masks as well as its main parameters: width Δ_m and height Δh (fixed invariants). This mask can be formalized as a complex-valued transfer function:

$$M(n,m) = exp(j\phi_{n,m}), \tag{2}$$

where $\phi_{n,m}$ is magnitude of phase-delay taken as binary random with equal probabilities for 0 and $\Delta\varphi_m$, corresponding to the height of the pixel Δh.

The Rayleigh-Sommerfeld model stands for wavefront propagation, in which the angular spectrum (AS)[30] method is defined as:

$$u(x,y,d) = \mathfrak{F}^{-1}\left\{ H(f_x, f_y, d) \cdot \mathfrak{F}\left\{ u(x,y,0) \right\} \right\}, \tag{3}$$

$$H\left(f_x, f_y, d\right) = \begin{cases} exp\left[i\frac{2\pi}{\lambda}d\sqrt{1-\lambda^2\left(f_x^2+f_y^2\right)}\right], & f_x^2+f_y^2 \leq \frac{1}{\lambda^2}, \\ 0, & otherwise. \end{cases} \tag{4}$$

Here $u(x, y, 0)$ is a wavefront in the initial plane, which propagates the distance d to create the diffractive wavefront $u(x, y, d)$. In Equation (3), $\mathfrak{F}$ and $\mathfrak{F}^{-1}$ determine the Fourier and inverse Fourier transform, $H(f_x, f_y, d)$ is the AS transfer function depending on the spatial frequencies f_x, f_y and the wavelength λ.

In systems without modulation, the captured intensity of a propagated wavefront does not provide enough details to reconstruct the object with high quality. The main idea behind our single-exposure system is to modulate this propagated wavefront, so the diffraction pattern will spread wider and provide more information on the object. Since the modulator mask is known, this additional information can be retrieved and used for reconstruction of the object transfer function. The advanced algorithm followed by this idea allows us to replace the traditional lens systems[4] by a compact binary phase-mask without any moving elements.

2.2 Super-resolution acquirement

The digital phase-retrieval technique requires to discretize physical wavefronts to calculate their propagation. These wavefronts on object-, mask-, and sensor planes may have different size features and, respectively, different sampling intervals Δ_o, Δ_m, and Δ_s, respectively.

However, it is convenient to use the same computational sampling rate Δ_c and computational pixel size $\Delta_c \times \Delta_c$ for all wavefronts and elements of the optical system, in particular, for the element-wise operations in Equation (1). The sampling rate of the continuous elements (phase-mask and object) can be arbitrary, therefore they are usually chosen to be equal to this value $\Delta_o = \Delta_m = \Delta_c$. The sampling rate on the sensor is limited by its' pixel size, so we can say that $\Delta_c = \Delta_s$, which means the conventional pixel-wise resolution of the captured diffraction pattern z.

For sub-pixel resolution, we may assume that the sensor pixels $\Delta_s \times \Delta_s$ are replaced by a smaller computational $\Delta_c \times \Delta_c$. In this way, the sensor diffraction pattern z can be treated as up-sampled with the sampling period Δ_c. If the resulting pattern $\tilde{z}$ has the computational pixels smaller than the physical sensor, $\Delta_c < \Delta_s$, and the reconstruction of the object is produced with Δ_c, we say about sub-pixel resolution (or super-resolution). The ratio $r_s = \Delta_s/\Delta_c > 1$ is called the upsamping factor.

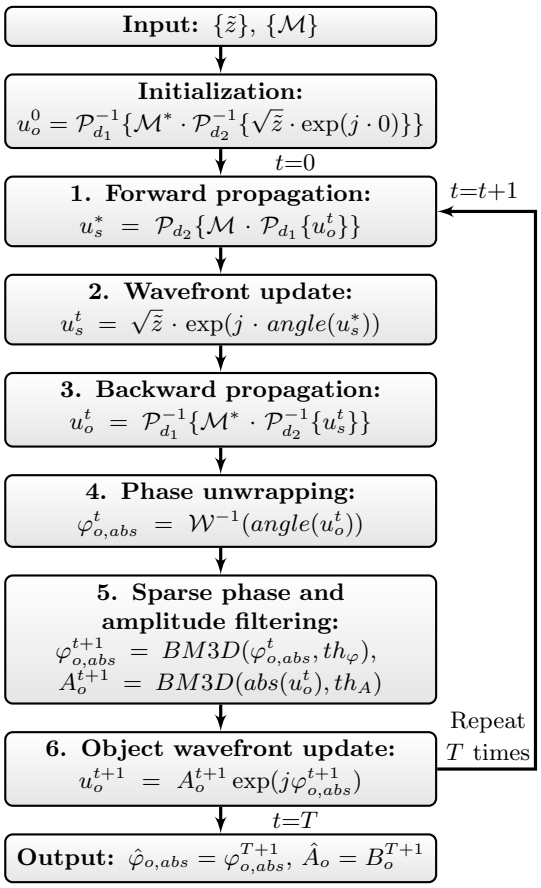

Figure 3. Flowchart of SR-SPAR method.

2.3 Block-Matching 3D filter

One of the important elements of the SR-SPAR algorithm is the BM3D filter[14] based on nonlocal self-similarity sparsity. It assumes that an examined image is containing multiple small similar patches. These similar patches are stacked together and form 3D arrays-groups (*grouping*). The 3D orthonormal transforms are applied to these 3D groups. The obtained transform 3D coefficients are hard-thresholded and then the inverse transform gives the 3D filtered groups. The filtered 2D patches of these groups are returned on their original positions in the image (*collaborative filtering*). As a result for each pixel of the image we may obtain more than one estimate. These estimates are aggregated by the weighted mean operation (*aggregation*). All these steps together define what is called the thresholding stage

of BM3D. The Wiener filtering is applied to the obtained filtered image as the second stage of BM3D. The Wiener filtering stage repeat grouping, collaborative filtering and aggregation steps described above with the only difference that the hard-thresholding is replaced by the Wiener filtering (more details in[14]).

The u_o complex wavefront can be determined as

$$u_o(x,y) = A_o(x,y) \cdot exp(i\varphi_o(x,y)), \tag{5}$$

where the A_o and φ_o stand for the object amplitude and phase. These two images are filtered by BM3D separately in order to exploit the sparse representation on real-valued variables, which result in $\hat{\varphi}_0$ and $\hat{A}_0$ estimates of phase and amplitude obtained as sparse approximations of the true unknown phase and amplitude:

$$\hat{\varphi}_o = BM3D(\varphi_o, th_\varphi), \tag{6}$$

$$\hat{A}_o = BM3D(A_o, th_A). \tag{7}$$

The BM3D algorithm is applied with the threshold parameters th_φ and th_A, respectively, for filtering phase and amplitude. To achieve the best resolution, these parameters are varying in iterations of SR-SPAR, taking smaller values in successive iterations.

The flowchart of the SR-SPAR algorithm can be seen in Fig. 3. The up-sampled captured intensity $\tilde{z}$ and the phase mask $\mathcal{M}$ are the inputs of the algorithm. A random initial guess for the object wavefront u_o^0 is propagated forward to the sensor plane (*Step 1*), where the amplitude is updated by the square root of $\tilde{z}$ (*Step 2*). This updated wavefront u_s^t is then propagated back to the object plane (*Step 3*) resulting in an improved object wavefront u_o^t. The $\mathcal{P}_d^{-1}\{u\}$ stands for the inverse of Equation (3), and $\mathcal{M}^*$ is the complex conjugate of $\mathcal{M}$. If the absolute phase range is higher than 2π, an unwrapping algorithm is needed in order to achieve correct reconstruction (*Step 4*). The phase $\varphi_{o,abs}^t$ and amplitude $abs(u_o^t)$ are BM3D filtered separately (*Step 5*) and they are merged together to produce an updated complex wavefront u_o^{t+1} (*Step 6*).

3. SIMULATION EXPERIMENTS

3.1 Main parameters and test images

In the experiments, we set the parameters simulating the prototype of physical system, inter alia, laser source with the wavelength of 532 nm, three type of test objects (Fig. 4), a phase-mask, and a CMOS sensor with the pixel size of 3.45 μm, maximum resolution of 2448×2048 and dynamic range of 12 bit. We assume that the mask phase-delay is $\Delta\varphi_m$ (Fig. 2) plus the object phase should be less than 2π to avoid the phase wrapping effects. The object's magnitude of phase-delay can be arbitrary, so we chose it to be $\Delta\varphi_o = \pi/2$ and the mask's $(\Delta\varphi_m)$ were chosen via simulation experiments in Sec. 3.2.

In general, the propagation requires matrices of the same size, therefore the wavefronts in each plane have to be zero-padded to correspond to the mutual size. To assign this value an initial intensity is calculated with pixel-wise resolution ($\Delta_s = \Delta_c$), which has to correspond to $r_s \cdot N_s$ sensor size, where r_s is the super-resolution factor, and $N_s \times N_s$ is the number of the sensor pixels. In case of sensor sub-pixel resolution ($r_s > 1$), we simulate the sensor pixel size Δ_s by averaging $r_s \times r_s$ computational pixels Δ_c.

Figure 4. Phase images used in simulation tests (from left to right): binary USAF target, continuous *cameraman* and *cell*.

Since we have to discretizate Equation (3) a restriction occurs, which limits the minimum number of the efficient sensor pixels N_{eff} according to the maximum distance ($d = d_1 + d_2$), the computational pixel size Δ_c and the wavelength λ. The inequality to calculate this minimum value based on previous researches[31,32] and can be written as

$$r_s \cdot N_s \geq N_{eff} = d\lambda/\Delta_c^2. \tag{8}$$

The phase-only USAF target is considered as a binary object to measure the resolving power of our system, the grayscale *cameraman* and *cell* images are used for continuous phase-imaging with the their pixel size chosen to be always equal to the computational pixel size ($\Delta_o = \Delta_c$).

The accuracy of the reconstructed images are measured by relative root-mean square error (RRMSE) between the true and reconstructed object's models as

$$RRMSE = \frac{\|\varphi_o - \hat{\varphi_o}\|_F}{\|\varphi_o\|_F}, \tag{9}$$

where φ_o and $\hat{\varphi_o}$ are the phases of the true and reconstructed object, and $\|\cdot\|_F$ means the Frobenius norm.

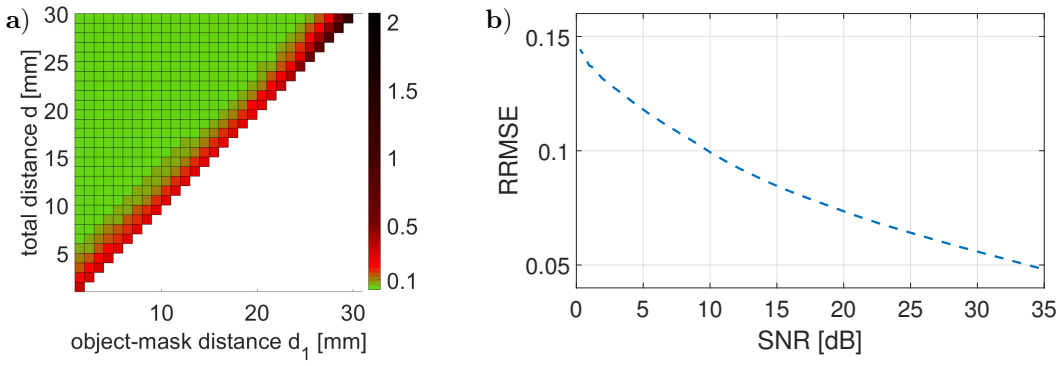

Figure 5. RRMSE of the reconstruction a) in different distances, b) in different noise-level

The tuning of distance parameters includes simulations assuming fixed object position, while the sensor is placed in the distance d from it. Then the mask is positioned between them taking distance values from the object (d_1) from 0 to d with the step of $1mm$. The effect on RRMSE of different mask and sensor positions, has been tested by using *cameraman* object for pixel-wise reconstruction. The error of reconstructions using these distances are shown in Fig. 5(a). The colors indicate the RRMSE values: green colors are the acceptable reconstructions with $RRMSE \leq 0.11$, reddish colors are not acceptable reconstructions with $RRMSE > 0.11$, and there are no values in the white area. We can see that positioning the mask too close to the sensor ($d - d_1 \leq 6mm$) prevents the efficient diffraction, resulting in information loss and imaging accuracy drop. In other hand, it is beneficial to choose both distances as small as possible, so we can ensure that all the diffractive frequencies are collected by the sensor. Considering these restrictions we selected the distance between the object and the mask as $d_1 = 2\ mm$ (as sum of $1mm$ gap and $1mm$ mask width), and the total distance between the object and sensor as $d = 17\ mm$ (as sum of d_1, $1mm$ gap and $14mm$ CS-mount).

The effect of different noise-levels was measured by calculating RRMSE for pixel-wise reconstruction of *cameraman* (Fig. 5(b)). Our method provided good results ($RRMSE < 0.11$) with 7 dB signal-to-noise ratio (SNR), which proves the system's noise-robustness.

3.2 Mask selection

Selection of the mask parameters (magnitude of phase-delay $\Delta\varphi_m$ and mask pixel size Δ_m) is based on the tests for three objects with highly different properties: a self-made USAF target with the smallest line-pair of 2 pixels, and two built-in Matlab images *cameraman.tif* and *cell.tif*. RRMSEs (Equation (9)) using masks of

different phase magnitude $\Delta\varphi_m$ were calculated in pixel-wise resolution and shown in Fig. 6(a). The results are 2π periodic and highlight, that the best performance is achieved at $\Delta\varphi_m = \pi$.

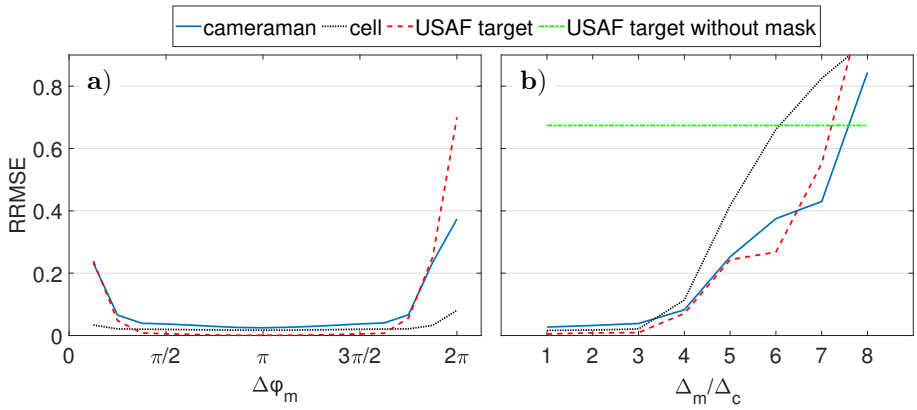

Figure 6. RRMSE of the objects (cameraman, cell, USAF target) reconstructed with phase-masks of different magnitude of $\Delta\varphi_m$ (a) and of different mask pixel size Δ_m with fixed computational pixel size Δ_c (b). Mask-less reconstruction of the USAF target (green) is shown for reference.

Keeping this value for $\Delta\varphi_m$, in Fig. 6(b) we examine the effect of the different mask pixel sizes ($\Delta_m/\Delta_c \geq 1$). The simulations are calculated in sensor sub-pixel resolution with super-resolution factor of $r_s = 2$. The results are showed in Fig. 6(b) and assigned that the smaller mask pixel size gives more accurate results.

In the previous research,[23] the phase-mask was realized on phase SLM with significantly larger pixel size than the sensor ($r_m \approx 36$), causing information loss, therefore to achieve the desired resolution multi-exposure technique with several different masks have to be applied.

4. SUPER-RESOLUTION DEMONSTRATION

4.1 Binary image

We present here simulations with the USAF target to examine the super-resolution limits of our method. The mask pixel size was chosen to be equal to the smallest detail of the object we would like to resolve $\Delta_m = \Delta_o$.

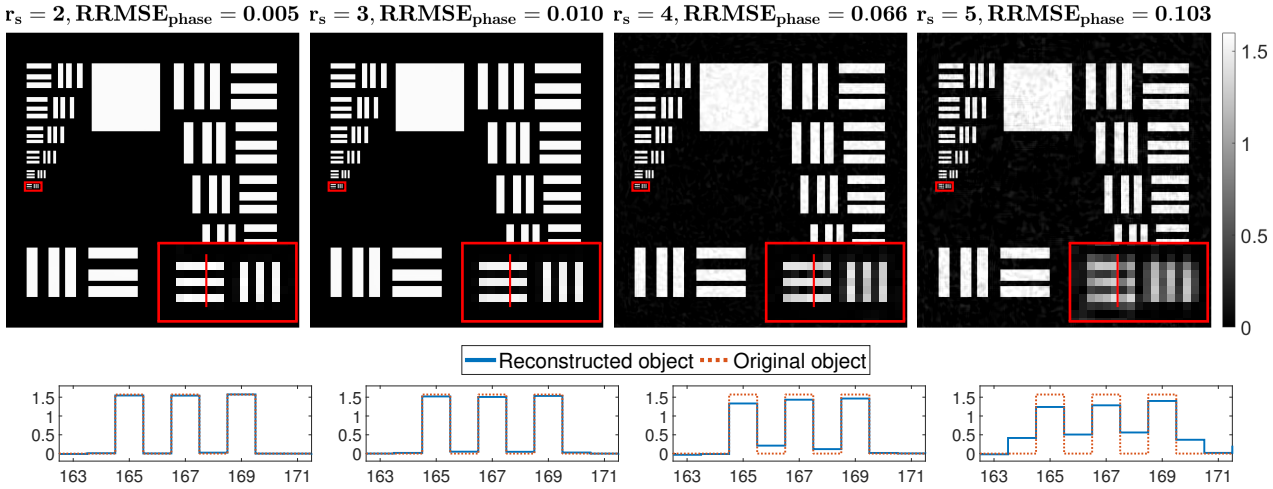

Figure 7. USAF target phase reconstructions with super-resolution factor r_s from 2 to 5, and the cross-sections of the smallest resolved target groups.

The reconstructed phase images and their cross-sections can be seen in Fig. 7. The method can provide the high-quality resolution even for $r_s = 4$, and can still resolve the target details which are 5-times smaller than the sensor pixel. Comparing our best super-resolution result $\Delta_s/5 = 0.69\ \mu m$ with the diffraction limited resolution Δ_{Abbe}, calculated by Abbe's criterion as

$$\Delta_{Abbe} = \frac{\lambda}{NA} \approx \frac{2d\lambda}{N\Delta_s} = 2.56\ \mu m, \tag{10}$$

we may conclude, that our technique allows to demonstrate 4-times better resolution (0.69 vs 2.56 μm). In Equation (10), NA stands for the numerical aperture, $\lambda = 532\ nm$ is the wavelength, $d = d_1 + d_2$ is the total distance from the object to the sensor. The sensor's dimensions are $N_s \times M_s = 2448 \times 2048$ and pixel size $\Delta_s = 3.45 \mu m$.

4.2 Continuous imaging

Using USAF target is one of the most efficient way to measure the resolving ability of a method, since it is a calibrated binary object. Real life objects are mainly continuous. We use continuous images (*cameraman* and *cell)* as phase-only objects to provide more evidence of quality imaging. All parameters are kept the same and the results for different super-resolution factors are shown in Fig. 8 and Fig. 9.

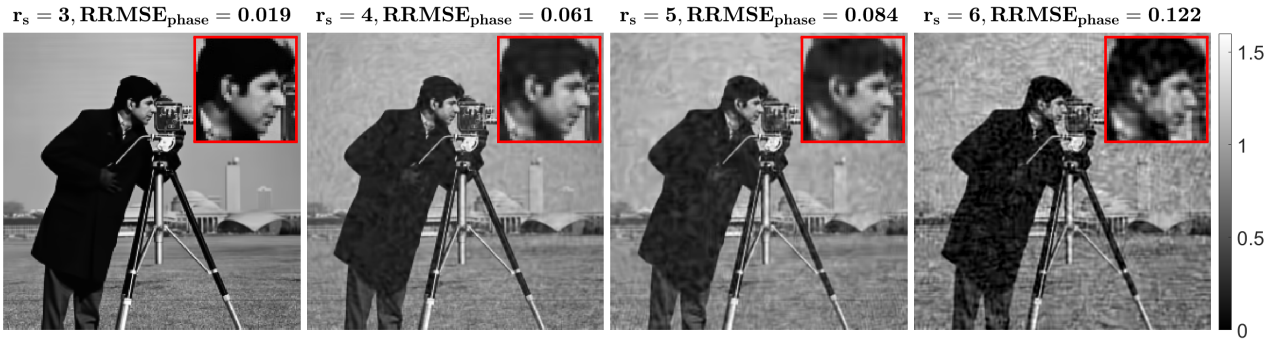

Figure 8. Quality imaging of continuous phase-only *cameraman* object with the super-resolution factor of 3 to 6.

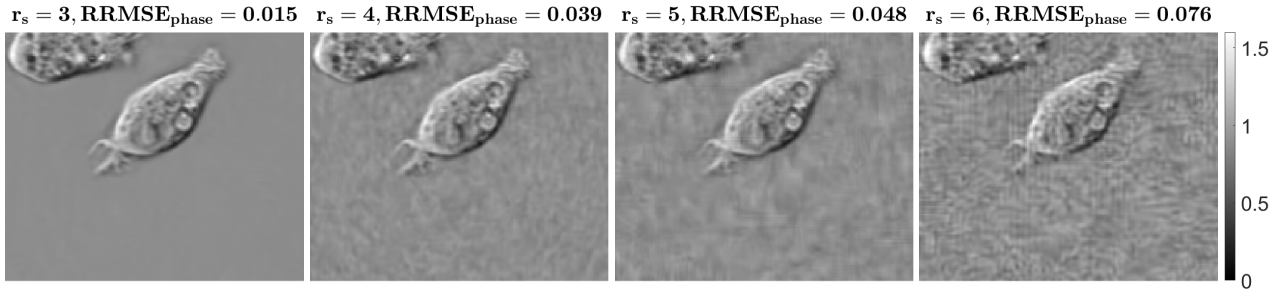

Figure 9. Quality imaging of continuous phase-only *cell* object in super-resolution factor of 3 to 6.

The obtained images and RRMSE values correspond well to Fig. 7. The system can provide outstanding quality for the super-resolution factor of 4, acceptable on factor 5, and the details are still distinct for factor 6. The result with pixel size of $\Delta_s/6 = 0.575\ \mu m$ corresponds to almost wavelength resolution ($\lambda = 0.532\ \mu m$) and compering to the diffraction limited resolution $\Delta_{Abbe} = 2.56\ \mu m$ (Equation (10)) we can see outstandingly better resolution capability.

5. CONCLUSION

A single exposure super-resolution lensless phase retrieval method was improved for quality imaging in sensor sub-pixel level. The system development included phase-mask selections, optimization of distances between object, mask, and sensor, and optimization of a sparse filtering in the iterative cycle. We successfully applied the SR-SPAR algorithm to reconstruct test objects in sub-pixel level from 2 to 6, the efficiency is verified by simulations, providing the resolved target with super-resolution factor of 6, retrieving details 4 times smaller than Abbe-limit. The simulations also showed that the smaller the mask pixels are the better the resolution will be.

As further work physical implementation of the system is planned. For this purpose a precise phase-mask will be manufactured and used for sub-pixel reconstructions of phase objects.

ACKNOWLEDGMENTS

Jane and Aatos Erkko Foundation and Finland Centennial Foundation funded Computational Imaging without Lens (CIWIL) project. Academy of Finland, project no. 287150, 2015-2019.

REFERENCES

[1] Wang, L. V. and Wu, H.-i., [Biomedical optics: principles and imaging], John Wiley & Sons (2012).
[2] Pawley, J., [Handbook of biological confocal microscopy], Springer Science & Business Media (2010).
[3] Gabor, D., [A new microscopic principle], Nature Publishing Group (1948).
[4] Fienup, J. R., "Phase retrieval algorithms: a comparison," Applied optics **21**(15), 2758–2769 (1982).
[5] Gerchberg, R. W., "A practical algorithm for the determination of phase from image and diffraction plane pictures," Optik **35**, 237–246 (1972).
[6] Yang, G.-z., Dong, B.-z., Gu, B.-y., Zhuang, J.-y., and Ersoy, O. K., "Gerchberg–saxton and yang–gu algorithms for phase retrieval in a nonunitary transform system: a comparison," Applied optics **33**(2), 209–218 (1994).
[7] Claus, D., Pedrini, G., and Osten, W., "Iterative phase retrieval based on variable wavefront curvature," Applied optics **56**(13), F134–F137 (2017).
[8] Almoro, P., Pedrini, G., and Osten, W., "Complete wavefront reconstruction using sequential intensity measurements of a volume speckle field," Applied optics **45**(34), 8596–8605 (2006).
[9] Lin, Y.-c., Chen, H.-C., Tu, H.-Y., Liu, C.-Y., and Cheng, C.-J., "Optically driven full-angle sample rotation for tomographic imaging in digital holographic microscopy," Optics letters **42**(7), 1321–1324 (2017).
[10] Petrov, N. V., Bespalov, V. G., and Gorodetsky, A. A., "Phase retrieval method for multiple wavelength speckle patterns," in [Speckle 2010: Optical Metrology], **7387**, 73871T, International Society for Optics and Photonics (2010).
[11] Katkovnik, V., Shevkunov, I., Petrov, N. V., and Egiazarian, K., "Multiwavelength surface contouring from phase-coded noisy diffraction patterns: wavelength-division optical setup," Optical Engineering **57**(8), 085105 (2018).
[12] Camacho, L., Micó, V., Zalevsky, Z., and García, J., "Quantitative phase microscopy using defocusing by means of a spatial light modulator," Optics express **18**(7), 6755–6766 (2010).
[13] Kohler, C., Zhang, F., and Osten, W., "Characterization of a spatial light modulator and its application in phase retrieval," Applied optics **48**(20), 4003–4008 (2009).
[14] Dabov, K., Foi, A., Katkovnik, V., and Egiazarian, K., "Image denoising by sparse 3-d transform-domain collaborative filtering. image processing, ieee transactions on 16 (8), pp. 2080-2095," (2007).
[15] Katkovnik, V. and Astola, J., "High-accuracy wave field reconstruction: decoupled inverse imaging with sparse modeling of phase and amplitude," JOSA A **29**(1), 44–54 (2012).
[16] Katkovnik, V. and Astola, J., "Sparse ptychographical coherent diffractive imaging from noisy measurements," JOSA A **30**(3), 367–379 (2013).
[17] Gerchberg, R., "Super-resolution through error energy reduction," Optica Acta: International Journal of Optics **21**(9), 709–720 (1974).

[18] Joyce, L. S. and Root, W. L., "Precision bounds in superresolution processing," JOSA A **1**(2), 149–168 (1984).

[19] Kirkland, A., Saxton, W., Chau, K.-L., Tsuno, K., and Kawasaki, M., "Super-resolution by aperture synthesis: tilt series reconstruction in ctem," Ultramicroscopy **57**(4), 355–374 (1995).

[20] Gustafsson, M. G., "Surpassing the lateral resolution limit by a factor of two using structured illumination microscopy," Journal of microscopy **198**(2), 82–87 (2000).

[21] Rivenson, Y., Stern, A., and Javidi, B., "Single exposure super-resolution compressive imaging by double phase encoding," Optics express **18**(14), 15094–15103 (2010).

[22] Agrawal, A. and Raskar, R., "Resolving objects at higher resolution from a single motion-blurred image," in [2007 IEEE Conference on Computer Vision and Pattern Recognition], 1–8, IEEE (2007).

[23] Katkovnik, V., Shevkunov, I., Petrov, N. V., and Egiazarian, K., "Computational super-resolution phase retrieval from multiple phase-coded diffraction patterns: simulation study and experiments," Optica **4**(7), 786–794 (2017).

[24] Kocsis, P., Shevkunov, I., Katkovnik, V., and Egiazarian, K., "Single exposure lensless phase imaging," EUVIP Workshop 2018 (2018).

[25] Rostykus, M., Rossi, M., and Moser, C., "Compact lensless subpixel resolution large field of view microscope," Optics letters **43**(8), 1654–1657 (2018).

[26] Bernet, S., Harm, W., Jesacher, A., and Ritsch-Marte, M., "Lensless digital holography with diffuse illumination through a pseudo-random phase mask," Optics Express **19**(25), 25113–25124 (2011).

[27] McLeod, E., Luo, W., Mudanyali, O., Greenbaum, A., and Ozcan, A., "Toward giga-pixel nanoscopy on a chip: a computational wide-field look at the nano-scale without the use of lenses," Lab on a Chip **13**(11), 2028–2035 (2013).

[28] McLeod, E. and Ozcan, A., "Microscopy without lenses," Phys. Today **70**(9), 50–56 (2017).

[29] Shevkunov, I., Katkovnik, V., Petrov, N. V., and Egiazarian, K., "Super-resolution microscopy for biological specimens: lensless phase retrieval in noisy conditions," Biomedical optics express **9**(11), 5511–5523 (2018).

[30] Goodman, J. W., [Introduction to Fourier optics], Roberts and Company Publishers (2005).

[31] Verrier, N. and Atlan, M., "Off-axis digital hologram reconstruction: some practical considerations," Applied optics **50**(34), H136–H146 (2011).

[32] Doval, Á. F. and Trillo, C., "Dimensionless formulation of the convolution and angular spectrum reconstruction methods in digital holography," in [Speckle 2010: Optical Metrology], **7387**, 73870U, International Society for Optics and Photonics (2010).